Recent advances in 3.5 μm Erbium Doped Mid-Infrared Fiber Lasers

Ori Henderson-Sapir, *Member, IEEE*, Andrew Malouf, Nathaniel Bawden, Jesper Munch, Stuart D. Jackson, *Senior Member, IEEE*, David J. Ottaway

(Invited Paper)

***Abstract*—The performance of mid-infrared Er^{3+}-doped fiber lasers has dramatically improved in the last few years. In this paper we present an overview of the progress in 3.5 μm fiber lasers based on the dual-wavelength pumping approach. The cross-section of the excited state absorption transition used by the 1973 nm second pump is found experimentally. A numerical simulation of the expected Q-switched behavior of this fiber laser is presented. This shows that increasing the power of the 977 nm pump is important to achieve high peak power pulses.**

***Index Terms*—Laser, fiber, optics, optical, infrared, mid-infrared, erbium, Er^{3+}, ZBLAN, numerical, model, simulation, optimization, 3.5 μm, 2.8 μm, dual-wavelength.**

I. Introduction

In this paper we review the current state of the art in rare-earth doped mid-infrared fiber lasers. The last decade has seen a continuing increase in the power available from mid-infrared sources. Significant attention has been given to sources such as optical parametric oscillators (OPOs) and amplifiers (OPAs), quantum cascade lasers (QC) and fiber lasers. The improvement in these sources have opened up many new possible applications in defense [1], environmental monitoring [2] and medicine [3]. Despite the advances, mid-infrared sources operating in the 3-4 μm band have lagged behind in terms of output power, portability, efficiency and beam quality.

Quantum cascade lasers have excelled at the longer wavelengths and the achievable wavelengths have recently been pushed further towards shorter wavelengths [4]. In recent years wavelengths as short as 3.2 μm have been demonstrated [5]. Compared with QCs, rare earth doped fiber lasers have the potential for efficient power scaling of high beam quality outputs. Moreover, their higher energy storage capability promises high peak powers, which are likely to be outside of QC capabilities. Recently, 3 μm fiber lasers have shown to exhibit power levels exceeding 30 W CW with peak powers exceeding 0.9 kW. [6], [7].

Infrared fiber lasers can now provide output over most of the wavelength range of 1-4 μm as can be seen in Fig. 1. The figure depicts the maximum average power demonstrated to-date from rare-earth doped fiber lasers. Originally, published in a review paper by Jackson [8] and updated for this paper it shows the state-of-the-art power achieved by fiber lasers at various wavelengths. It also demonstrates that until recently the output power versus wavelength follows a trend line that decreases exponentially with increasing wavelength until 3 μm, above which the laser power fell significantly to 10 mW.

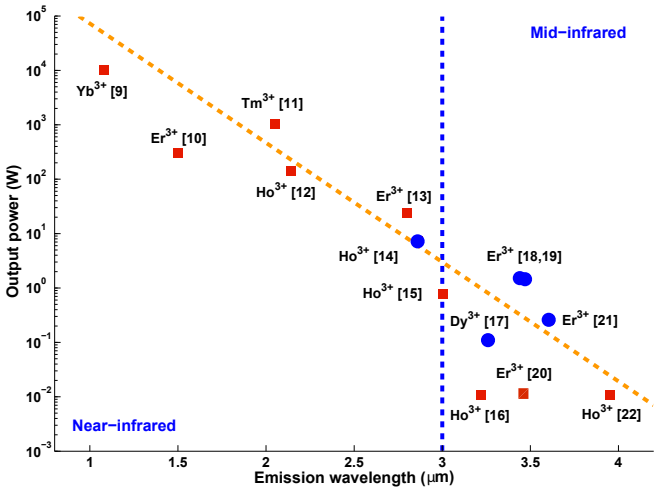

Fig. 1. Published laser power from rare-earth doped fiber laser as a function of operating wavelength [9]–[22]. The trend of reduced power as the wavelength increases (dashed orange line) is mostly a result of the energy difference between pump and laser photons. Recent development since 2012 [8] are marked with a blue circle. The Ho^{3+} based 3.9 μm laser required cryogenic cooling [22].

The pioneering work done on demonstrating fiber lasers with wavelengths longer than 3 μm was done by a group from the Technischen Universität Braunschweig in Germany in the 1990's. They demonstrated lasers that operated at 3.2 μm [16] and 3.9 μm (cryogenically) [22] using Ho^{3+}:ZBLAN fiber and at 3.5 μm [20] using Er^{3+}:ZBLAN fiber. These lasers had high threshold and low slope efficiencies, particularly when operated at room temperature. The maximum average power levels were at the 10 mW level.

The low powers and efficiencies demonstrated previously in these lasers can be attributed to the following reasons. First, the high phonon energy of silica glass means that it is not transparent beyond 2.4 μm and longer wavelength transitions are efficiently quenched by multi-phonon non-radiative decay. This requires the use of more exotic glasses, such as the fluoride glass ZBLAN which are less mechanically

Manuscript received June xx, 2016; revised June xx, 2016. This work was supported by the South Australian Premier Research and Industry Fund (PRIF) Grant.

O. Henderson-Sapir, A. Malouf, Nathaniel Bawden, J. Munch and D. Ottaway are with The University of Adelaide, Adelaide, S.A. 5005, Australia (email: david.ottaway@adelaide.edu.au). S. Jackson is with Macquarie University, NSW 2109 Australia, (email: stuart.jackson@mq.edu.au).

robust and have proven more difficult to fabricate and handle. In addition, many of the longer wavelength transitions are located high above the ground state, which means the lasing transition is inherently inefficient due to high quantum defect. Moreover,excited states located below the lasing transition often have long radiative lifetimes which are fully realized due to the required low phonon energy of the glass hosts. These long lifetimes trap ions and prevent them from returning to the ground state after lasing which depletes the ground state and reduces pump absorption. Therefore, the high quantum defect for the longer transitions, combined with less mature glasses and compounded by less efficient pump sources [23] are the main reasons behind the declining trend in laser power shown in Fig. 1. In the case of the ${}^4F_{9/2} \rightarrow {}^4I_{9/2}$ transition in erbium [20] we have recently found evidence that the high threshold in these experiments were likely caused by an energy exchange process that robs the top lasing state of ions [24].

We realized that the long-lived lower level excited states could be transformed from a hindrance to an advantage if they were used to significantly reduce the quantum defect of these laser. This could be achieved using dual-wavelength pumping (DWP) whose concept is illustrated in 2. Dual wavelength pumping uses one pump wavelength (P_1) to establish a population in one of the long-lived excited states which we have called a "virtual ground state". The lasing cycle then consists of pumping the ions to the top lasing state using a second pump (P_2), post-lasing the ions return to the virtual ground state and the cycle is repeated. In this way ions can undertake this lasing cycle a number of times before they drop to the ground state and need to be re-pumped to the virtual ground state using P_1. This technique offers the additional benefit of using infrared pump wavelengths that are more readily available at higher powers than the visible sources required for direct ground state pumping. Our initial work demonstrated this concept on the ${}^4F_{9/2} \rightarrow {}^4I_{9/2}$ transition in erbium [21], [25], [26]. Our first demonstration of mid-infrared DWP laser significantly surpassed the 10 mW barrier, achieved a slope efficiency of 25 % and brought the 3.5 μm Er^{3+} transition onto the trend line shown in Fig. 1. Further power scaling to 1.5 W output power was demonstrated recently by our group [19] and the Université Laval group [18] who used an all fiber approach.

We expect that further power scaling of the 3.5 μm transition is achievable. To facilitate this we have recently finished a numerical model that emulates the 3.5 μm system [27]. This numerical codes allows us to simulate different conditions and various geometries prior to committing to purchase costly ZBLAN fibers. Moreover, our code allows us to investigate both the spatial and temporal development of the laser pulse along the fiber, therefore enabling the investigating of gain-switching and Q-switching. Both short pulse approaches are necessary for remote sensing applications and might allow 3.5 μm fiber lasers to replace costly OPOs as laser sources for remote sensing applications.

Results from Figs. 1 and Fig. 3, together with the results from Braunschweig Group [22] demonstrate that fiber lasers can span the entire 2.6-3.9 μm wavelength range, which covers the important light absorption "fingerprint" range of many organic compounds, some of them shown in Fig. 4. This development can open new applications for fiber lasers in spectroscopy that were not previously available.

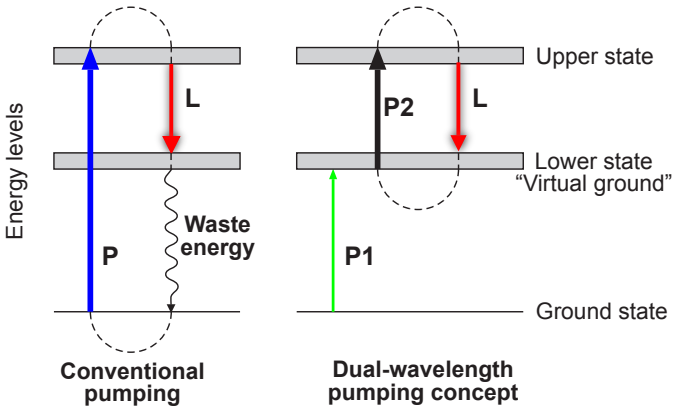

Fig. 2. The dual-wavelength pumping concept compared to ordinary ground-state based pumping.

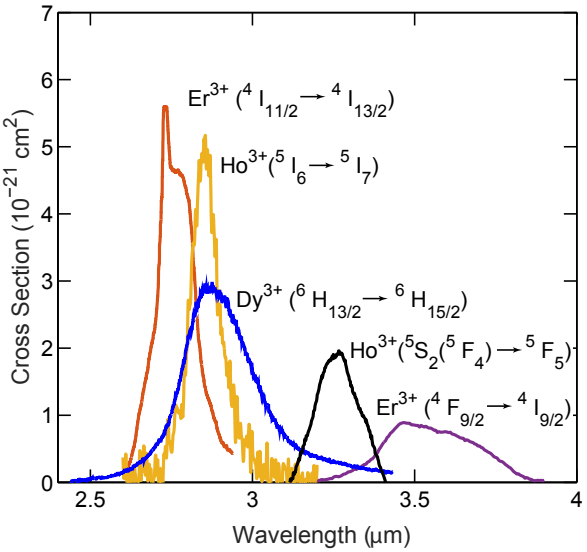

Fig. 3. Emission cross-sections of mid-infrared transitions in rare-earth doped ZBLAN glass. The 3.2 μm cross-section was calculated from the spontaneous emission spectrum in [16] in conjunction with spectroscopic data from [28] by applying the Fuchtbauer-Ladenburg method [29].

In this paper we describe new experimental and modeling results which are important for improving the performance of DWP based 3.5 μm fiber lasers. First we show the optimal wavelength for the excited state pump source (P_2) in a DWP system is 1973 nm. We then present our experimental work to find the absorption and emission cross-sections curves associated with the second pump source.

In the following section we show phenomenologically that the emission spectra at the 3.5 μm band has a considerable dependence on the source of the ZBLAN glass used and its doping concentration which has ramifications for extending the tuning range of this transition. We conclude by presenting a numerical analysis of a Q-switched DWP, 3.5 μm laser which

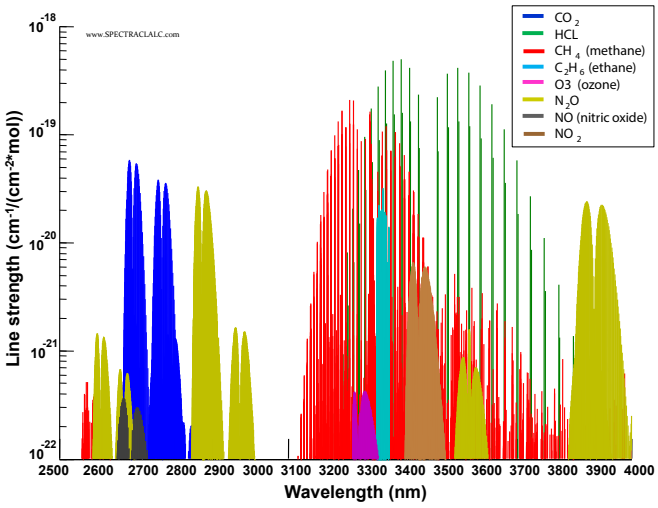

Fig. 4. Absorption of various gasses in the 2.5-4 μm spectral range. Note that the three most important greenhouse gases, water (not shown for brevity - many lines), carbon-dioxide and methane, are all present.

is a necessary precursor for the evaluation of high peak-pulse lasers in this band for laser based remote sensing applications.

II. 2 µM EMISSION CROSS-SECTION

To achieve efficient pumping of the DWP system by the second pump, it is important that its wavelength is close to the peak absorption of this transition ($^4I_{11/2} \rightarrow ^4 F_{9/2}$) (see Fig. 5). In this section we present measurements using excited state spectroscopy to determine the relevant excited state cross-section for the first time in Er^{3+}:ZBLAN. Spectroscopic data available from Caspary [30], suggests that the transition has a zero-phonon transition wavelength of 1973 nm and no ground state-absorption (GSA) or excited-state absorption (ESA) transitions correspond to this wavelength band suggesting little interference in the measurements from other transitions. Existence of a weak excited-state absorption that originates from the $^4F_{9/2}$ state has been proposed by the Laval group [31] to explain their modeling results. This excited state absorption will not effect the results presented here because a significant population is not established in the $^4F_{9/2}$ state. The experimental set-up used to perform this measurement is illustrated in Fig. 6.

Determining the optimum ESA wavelength using a fiber compared with bulk has two major advantages. The increased interaction length allows small cross-sections to be measured and the fiber geometry ensures good spatial overlap between the probe beam and the excited state population established by the 974 nm pump. For the fiber experiments, we used a commercially available Er^{3+} doped ZBLAN fiber manufactured by FiberLabs. The fiber had a 3.6 μm core with an NA $= 0.28$ and 125 μm diameter cladding surrounded by polymer coating with 250 μm diameter. The doping concentration was low, 8×10^{19} $ions/cm^3$ or 0.5 mol% to minimize non-radiative energy transfer processes.

We determined the lineshape of the ESA transition using the experimental set-up illustrated in 6. Light from a 974 nm diode and a broadband supercontinuum source (SCS) was

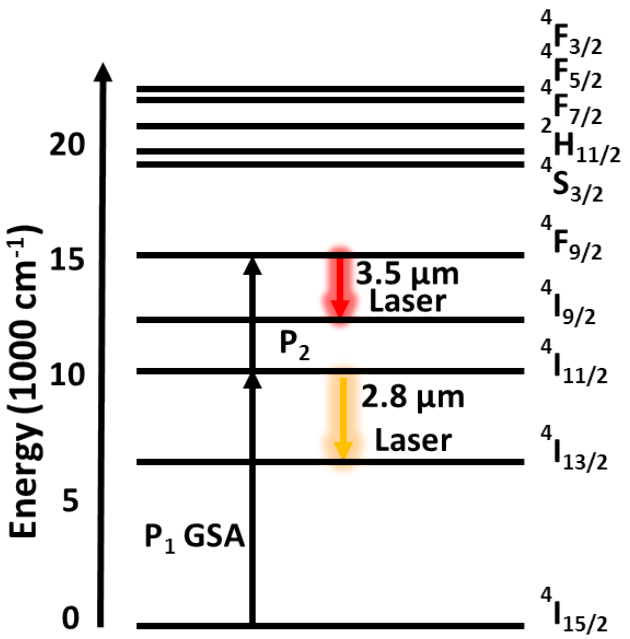

Fig. 5. Energy level diagram of Er:ZBLAN

launched into an Er^{3+}:ZBLAN fiber. The 974 nm diode excited ions from the ground state and created a population at the $^4I_{11/2}$ level. The SCS probed the $^4I_{11/2} \rightarrow ^4 F_{9/2}$ transition at a variety of wavelengths to determine a relative transmission over a wideband wavelength for a range of differing 974 nm pump powers. By determining the spatially averaged population of the $^4I_{11/2}$ level, this absorption spectra was used to calculate the absolute excited-state absorption cross-section.

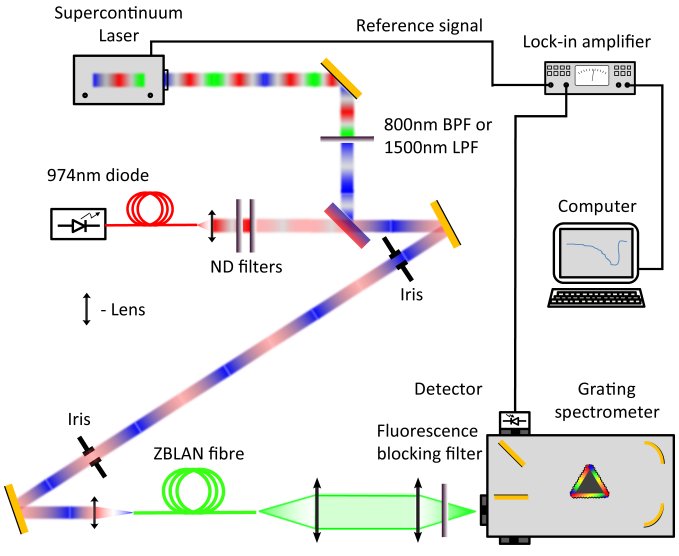

Fig. 6. Experimental setup for in-fiber pump-probe measurement for determining $^4I_{11/2} \rightarrow ^4F_{9/2}$ transition cross-section. BPF - bandpass filter, LPF - longpass filter. For further details, see text.

In this experimental set-up, the pump and probe beams were launched into the fiber from the same direction. The pump

beam was a 330 mW, 974 nm single mode, fiber-coupled laser diode (Thorlabs PL980P330J), which was collimated using an aspheric lens. Some measurements required neutral density filters to attenuate the beam whilst maintaining a constant current and hence wavelength for the 974 nm laser diode.

The probe beam was generated by a Koheras SuprK supercontinuum source (SCS) with a power spectral density of 0.01 mW/nm in the band around 1970 nm. The single transverse mode output of the SCS enabled easy alignment and focusing into the fiber. The SCS was internally pulsed with a pulse duration of ~ 1 ns and a pulse repetition frequency (PRF) of 22.6 kHz. The TTL output from the SCS was used to synchronize the lock-in amplifier (LIA). Various filters were used to allow only a certain band of the SCS to be incident on the ZBLAN fiber.

The beam from the SCS was combined with the 974 nm beam on a 45° dichroic mirror (CVI Laser Optics). The dichroic mirror reflected the wavelength range of 1500-2400 nm while it transmitted the 974 nm beam. The combined beams were launched through an aspheric lens into the ZBLAN fiber. Chromatic dispersion of the launching aspheric lens resulted in large variations in launch efficiency at the different wavelengths used. This was especially noticeable when launching the 974 nm pump and the broadband SCS beam around 1900 nm band. The launching conditions were thus a trade-off between launched pump and probe power. This issue could be avoided in future experiments by using reflective focusing optics.

The launched beams interacted with the Er^{3+} ions by GSA and ESA transitions. The residual pump, probe and fluorescence emerging out of the fiber were collimated by an uncoated CaF_2 lens. Short wave fluorescence was filtered from the emerging beam using either a 1550 nm or 1150 nm longpass filter (Thorlabs). The remaining light was focused into the spectrometer (Princeton Instruments, Acton 2557) using an additional CaF_2 lens.

Visible and near-IR wavelengths were detected using a silicon photo-diode (Horiba DSS), while the 1970 nm band light was detected by an extended InGaAs biased photodiode detector (Thorlabs DET10D). The signal from the detector was fed into a LIA (Stanford Research System SRS830) for amplification and demodulation at the SCS frequency. The signal from the LIA was logged by computerized acquisition and control system (Princeton Instruments, SpectraHub).

An example of the change in the transmitted probe beam spectrum between 1500 nm and 2100 nm with changing 974 nm power is shown in Fig. 7. It shows a wide absorption band stretching between 1900 nm and 2020 nm, with its peak centered at 1973 nm. As expected, the depth of absorption was strongly dependent on the 974 nm power launched into the fiber.

In the case of a pump and probe measurement and following Pollnau et al. notation [32], the general case for the transmission ratio of a probe beam with and without a pump beam is

$$\frac{1}{N_e l}\ln\left(\frac{I_p}{I_u}\right) = \sigma_{GSA} + \sum_i \frac{N_i}{N_e}\left[\sigma_{SE}(i) - \sigma_{ESA}(i)\right]. \quad (1)$$

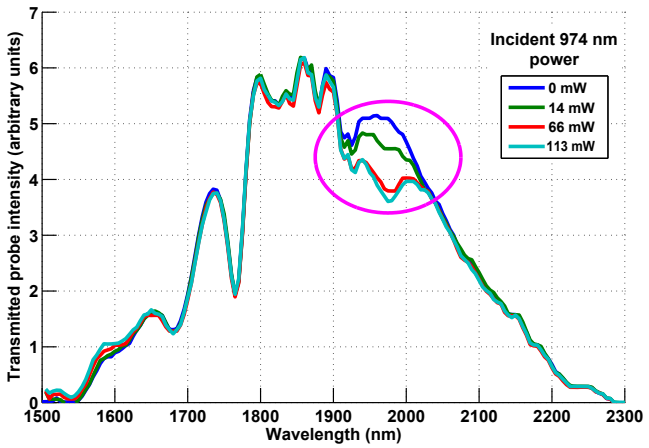

Fig. 7. Initial broadband transmission scan showing ${}^4I_{11/2} \rightarrow {}^4F_{9/2}$ ESA. The ellipse encompasses the ESA region of the 1973 nm absorption maximum. On the left side of the curves, we see hints of weak stimulated emission around the 1550 nm band.

In 1, we defined $N_e = \sum_i N_i$ as the total population density of all excited states, and the ratio of the transmitted probe power with the pump laser on and off is $(\frac{I_p}{I_u})$. σ_{GSA}, σ_{ESA} and σ_{SE} are the absorption cross-sections of the ground and excited state transitions and the stimulated emission (SE) cross-sections, respectively.

The excited state absorption spectra of Fig 7 was used to calculate the wavelength dependent cross-section for this transition using 2.

$$\sigma_{ESA} = \frac{1}{N_{4_{I_{11/2}}} l}\ln\left(\frac{I_p}{I_u}\right). \quad (2)$$

To determine the absolute cross-section, accurate measurements of the population of the ${}^4I_{11/2}$ state ($N_{4_{I_{11/2}}}$ in 2), the fiber length l and the probe beam transmission ratio $\left(\frac{I_p}{I_u}\right)$ are required . The last term is readily obtained from a transmission measurement since it is independent of absolute power. This holds as long as the power levels are kept low to prevent bleaching of the population established by the pump. Obtaining the $N_{4_{I_{11/2}}}$ term accurately is considerably more challenging since it requires an absolute value. The procedure for achieving this is described below.

It should be noted that 2 assumes that there are no neighboring excited state absorptions whose wings overlap the excited absorption of interest. The data shown in Fig 7, supported by the work of Caspary [30] shows that there are no significant ESA or SE bands which overlap the 1970 nm band. ESA and SE bands, which are further removed from the 1970 nm band can be identified in Fig 7. A feature close to 1550 nm was the result of the ${}^4I_{15/2} \rightarrow {}^4I_{13/2}$ GSA transition combined with SE on the ${}^2H_{11/2} \rightarrow {}^4I_{9/2}$ transition. This SE transition starts at 1470 nm but the short edge was not measured in the scan of Fig. 7, because of the 1500 nm longpass filter used to eliminate second order shorter wavelengths from coming through the spectrometer.

We used the following additional pump-probe experiment to obtain the average population of the ${}^4I_{11/2}$ state at each

974 nm power level. The transmission through the fiber of a weak 797 nm beam probed the ${}^4I_{15/2} \rightarrow^4 I_{9/2}$ GSA transition. This experiment provided an absolute average value for the change in the mean ground population of the fiber. We observed a change in the transmission of the 797 nm beam, due to the bleaching of the ground state, ${}^4I_{15/2}$ due to high pump intensity.

As stated previously, the ${}^4I_{11/2}$ population cannot be calculated simply by using the absorbed power of the 974 nm pump because this required a very accurate knowledge of the coupling efficiency. Further, the pump wavelength (974 nm) is known to drive a number of excited state processes which further complicates this relationship.

When the 974nm pump is switched on, the change in the ground population is

$$\begin{aligned}\Delta N_g &= N_{ground\,with\,pump} - N_{ground} = -N_e \\ &= -(N_{{}^4I_{13/2}} + N_{{}^4I_{11/2}} + N_{Higher}),\end{aligned} \tag{3}$$

where N_{Higher} is the population of all other excited states, beyond ${}^4I_{13/2}$, and ${}^4I_{11/2}$. N_{Higher} was small because of the combination of low pump power, low doping concentration and the short lifetimes of levels above ${}^4I_{11/2}$. In a case similar to ours, with CW 974 nm pumping Pollnau et al. showed numerically [33] that less than 1% of the population occupied levels above ${}^4I_{11/2}$. Hence, we disregard the N_{Higher} term in 3.

Pollnau et al. [33] also derived the ratio of population of the ${}^4I_{13/2}$ and ${}^4I_{11/2}$ levels to the total excited population and found that the population of these levels was dominated by the ratio of lifetimes of the energy levels. They found that this ratio held for doping densities up to almost 4 $mol\%$ doping of Er^{3+} ions [34], [35], which is considerably higher than the doping densities used in our experiment (0.5 $mol\%$). We therefore used their result for the excited state population ratio of 33% and 66% for the ${}^4I_{13/2}$ and ${}^4I_{11/2}$ levels' occupation, respectively. Using these results together with 3, we find

$$N_{{}^4I_{11/2}} \simeq -\frac{2}{3}(\Delta N_g). \tag{4}$$

The change in the ground state population can be measured by observing the change in transmitted light in the 800 nm band of the SCS, with and without the 974 nm pump operating. This change in transmission corresponds to absorption by the ${}^4I_{15/2} \rightarrow^4 I_{9/2}$ GSA transition and the relevant additional ESA transitions shown in reference 1.

$$\begin{aligned}N_{{}^4I_{11/2}} = \frac{1}{l}\ln\left(\frac{I_{out\,800nm\,pump}(\lambda_1)}{I_{out\,800nm}(\lambda_1)}\right) \\ \times \frac{1}{\frac{3}{2}\sigma_{GSA}(\lambda_1) - \frac{1}{2}\sigma_{ESA_{{}^4I_{13/2}}}(\lambda_1) - \sigma_{ESA_{{}^4I_{11/2}}}(\lambda_1)}\end{aligned} \tag{5}$$

Equation 5 holds so long as a significant population is not established in the ${}^4I_{9/2}$ state, which allows us to omit the stimulated emission term and obtain 5.

The combination of the low incident power of the SCS over the entire 800 nm band (0.2 mW) and short lifetime of the ${}^4I_{9/2}$ state (10 μs) ensures that this is true.

To determine the population of the ${}^4I_{11/2}$, it was necessary to know the GSA and ESA cross-sections for specific wavelengths. These cross-section were obtained from Pollnau et al. [33] ($\sigma_{GSA} = 6.7 \times 10^{-22}\,cm^2$, $\sigma_{ESA_{{}^4I_{13/2}}} = 11.6 \times 10^{-22} cm^2$ and $\sigma_{ESA_{{}^4I_{11/2}}} = 1.5 \times 10^{-22} cm^2$) at 797 nm. To maximize the signal-to-noise, we chose a wavelength within the 800 nm band where GSA is dominant. From the work of Pollnau [33], the peak of the GSA transition occurs around 797 nm. We conducted an additional pump-probe scan at this band which confirmed the wavelength of the peak of the GSA transition. The peak of the ${}^4I_{15/2} \rightarrow^4 I_{9/2}$ GSA transition was coincidentally at the intersection point of both ${}^4I_{13/2} \rightarrow^2 H_{11/2}$ and ${}^4I_{11/2} \rightarrow^4 F_{3/2}$ ESA transition cross-section curves. By using this wavelength, we were able to obtain the highest signal-to-noise and be least affected by ESA at the 800 nm band.

In the above derivation, all population densities are assumed to be the average values over the entire fiber length. The exponential absorption profile of the pump means that the local ion density at each position along the fiber is different. Under the assumptions of negligible effect of cross-relaxation (CR) and energy-transfer upconversion (ETU) processes and negligible loss in the fiber, the average ion densities are independent of the local population and depend only on the total pump power absorbed. These assumptions are believed to be valid in our case since the fiber used had low doping concentration and the pump power used was low, both minimizing the effects of CR and ETU processes.

The derivation by Pollnau et al. in [33] assumed that bleaching of the ground state was very limited. In their case, less than 15% of the population was in an excited state. In our case, due to the small core of the fiber, a large fraction of the population could be excited. Thus, in order to maintain the validity of the above derivation, it was necessary to reduce the pump power as much as possible while maintaining a reasonable signal to noise. The calculated ESA cross-section at 1973 nm was not accurate when using high 974 nm pump power which excited a significant fraction of the ion population.

After finding the ion density of the ${}^4I_{11/2}$ level with varying 974 nm pump power, a second measurement was performed using the same setup that was used to measure the 1973 nm absorption. From the transmission fraction and the ion population we could derive the absorption cross-section using 2.

The two experiments used a similar experimental setup to the one in Fig. 6 with slight variations. The 1500 nm longpass filter was replaced by an 800 nm bandpass filter for the first part of the experiment measuring the 800 nm transmission and was reverted back to the 1500 nm longpass filter for the second part of the experiment. A longer fiber, 65 cm long was used for both experiments to increase the absorption of the light and hence the signal level.

The absorption was linear up to about 25 mW of 974 nm

pump, where saturation effects started occurring. Beyond this point the bleaching of the ground state significantly changes the likelihood of GSA. Moreover, ESA becomes signficant at higher power levels due to increased population at higher levels than $^4I_{11/2}$ which causes the population ratio to deviate from one used to calculate 5.

By combining the results of the ion density from the 797 nm transmission measurement with the 1973 nm absorption at low pump powers a consistent cross-section of $\sigma_{1973nm} = 2.3 \pm 0.8 \times 10^{-21}\, cm^2$ was obtained. The relatively high uncertainty (30%) at these low power data arises from the lower signal-to-noise and instabilities of the SCS source.

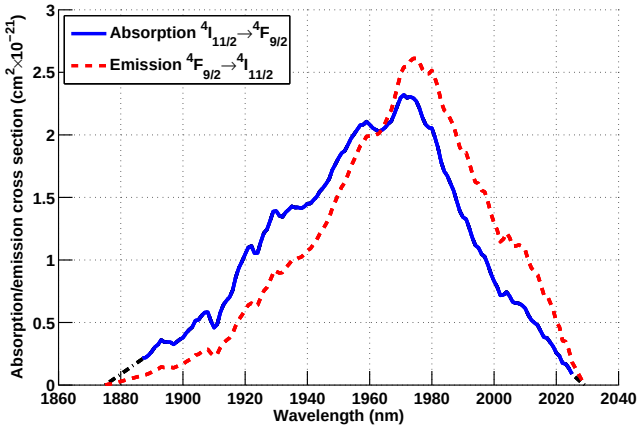

Fig. 8. ESA cross-section of the $^4I_{11/2} \rightarrow {}^4F_{9/2}$ transition based on measurement of bleaching of the ground. The black dot-dashed line represents extrapolation of the measured absorption data. Peak absorption cross-section value is $\sigma_{1973nm\ abs} = 2.3 \pm 0.8 \times 10^{-21}\ cm^2$ and emission peak value is $\sigma_{1973nm\ em} = 2.6 \pm 0.9 \times 10^{-21}\ cm^2$.

The emission cross-section of the $^4F_{9/2} \rightarrow {}^4I_{11/2}$ transition can be inferred from the absorption cross-section using the McCumber relation [36] and it is shown in Fig. 8. Energy of the appropriate Stark levels required for this calculation can be found in [37]. We arrived at a peak emission cross-section of $\sigma_e = 2.6 \pm 0.9 \times 10^{-21}\ cm^2$ with the wavelength dependency shown in Fig. 8. The value obtained of $\sigma_{1973nm} = 2.3 \pm 0.8 \times 10^{-21}\, cm^2$ is the first experimental value obtained for this ESA transition.

III. Variations in the 3.5 μM Emission Shape

In our previous work [19] we demonstrated a 450 nm wide tuning range on the transition centered on 3.5 μm band using the DWP method. Such wide tuning is significant to the future sensing of hydrocarbons which tend to have strong absorption lines closer to the short-wavelength edge of the tuning range illustrated in Fig. 9.

It is therefore imperative to ensure efficient operation at the shorter edge of the tuning range, which looks achievable since there is large variability in the fluorescence curves obtained from fibers made using slightly different compositions of ZBLAN and differing dopant concentrations. This is summarized in Fig. 10 which shows fluorescence curves obtained from four different fiber sources: Two fibers manufactured by FiberLabs, a single clad, 0.5 mol% fiber (ZSF) and a

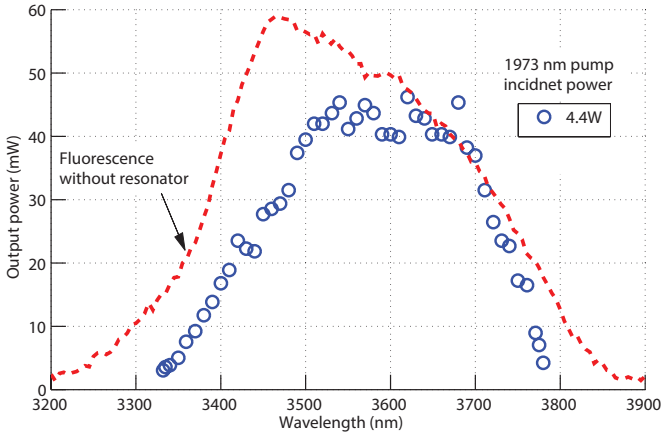

Fig. 9. Wavelength tuning obtained using 2.8 m long, 1 mol% Er^{3+}:ZBLAN fiber while employing the DWP method [19]. 5 W of 977 nm pump and 4.4 W of 1973 nm pump powers were used. The dashed line represents the fluorescence spectrum of the $^4F_{9/2} \rightarrow {}^4I_{9/2}$ without a resonator.

4 mol% double clad fiber (ZDF). A third fiber manufactured by LeVerre Fluore (1 mol%) and a forth one made by IR-Photonics (1.7 mol%). The fluorescence from these four fibers was collected during our work. A fifth fiber (1 mol%) single clad, is from the work of Többen [20]. The large differences of the short and long edges of the fluorescence cannot be attributed to slight differences in calibration as they span over 100 nm on each side. Although the different curves were collected from fibers of different lengths, this should not significantly affect the fluorescence profile because the cross section of the fiber is low and re-absorption by the sparsely populated $^4I_{9/2}$ level was negligible

The origin of the difference between the fibers is not clear. Fig. 10 suggests that doping concentration might contribute to the location of the short edge. Understanding the causes and controlling the location of the short edge is essential for future spectroscopy application since the strongest fundamental absorption lines involving C-H bonds fall around 3.34 μm, well within the wavelength region mostly affected by the fluorescence short-edge variations.

IV. Q-switching

Q-switching is a long established technique for producing short pulses with high peak power [38]. Such pulses are extremely useful in remote sensing applications such as differential absorption lidar (DiAL), see for example [39]. In this section we investigate the likely Q-switching behavior of a 3.5 μm fiber laser using our time domain numerical model [27]. We evaluate the laser performance using the same parameters that were used to demonstrate 1.5 W level power operation [19]. The laser gain medium was a 2.8 m long, 1 mol% doped Er^{3+}:ZBLAN fiber. This double-clad fiber had a core diameter of 16 μm and a circular, double truncated cladding of 240/260 μm. The numerical apertures of the core and inner cladding were 0.12 and 0.46 respectively. Both ends of the fiber were butted against dichroic mirrors. At the pump

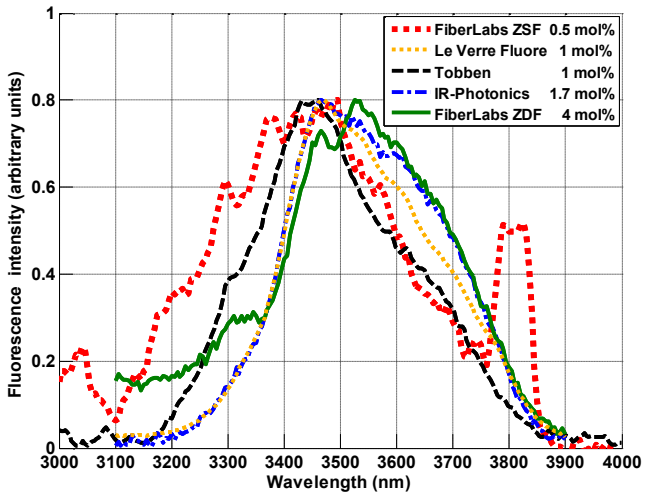

Fig. 10. Comparison of the normalize fluorescence from the ${}^4F_{9/2} \rightarrow {}^4I_{9/2}$ transition from different fiber varieties.The distinctive feature at 3820 nm in the FiberLabs ZSF curve is the result of stray light from the 1909 nm pump source.

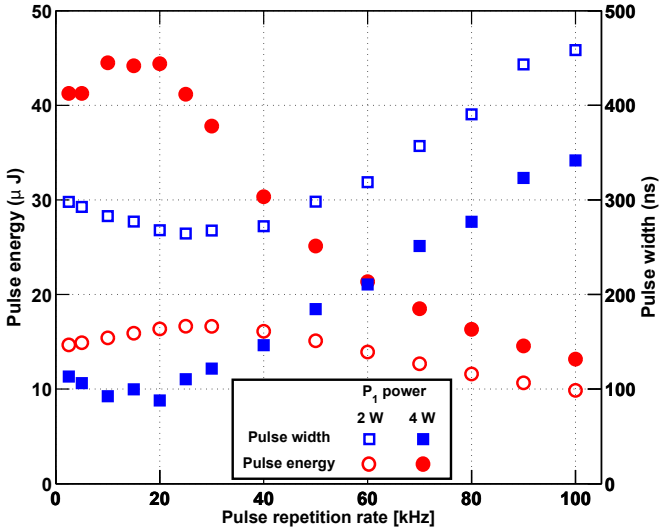

Fig. 11. Simulated pulse energy and pulse width for Q-switched operation using 2.8 m long, 1 mol% Er^{3+}:ZBLAN fiber while employing the DWP method. 2 W and 4 W of 977 nm pump and 5.5 W of 1973 nm pump powers were used. The Q-switching frequency was varied as part of the simulation.

input end, the mirror was 100% reflective at 3.5 μm while 80% and 90% transmissive at the 977 nm and 1973 nm pump wavelengths, respectively. The output dichroic was an 80% transmissive mirror at 3.5 μm.

This study presents results for the case where both pumps operate in CW modes suitable for high PRF remote sensing applications. Q-switching is simulated by repetitively switching the intra-cavity loss between high and low loss states. The switching time is modeled to be instantaneous and we show that build-up time of a pulse is in the order of microseconds. Therefore, slower switching times, such as those seen with acousto-optic type switches, would not alter the outcomes significantly.

We conducted a series of simulations to obtain a modeled Q-switched pulse train. Firstly, we performed 20 ms simulations with the power of the first (977 nm) pump set to 2 W and 4 W. This length of time is sufficient to reach a steady state population in the ${}^4I_{11/2}$ state (the "virtual ground state") which has a lifetime of 7.9 ms [35]. We then followed with further 20 ms simulations where the second (1973 nm) pump operated at 5.5 W (as used in our previous experiments [19]) and the Q-switch alternated between high and low loss states. The Q-switch on-time (low loss) was consistently 5 μs while the off-time (high loss) was determined by the PRF. This second simulation allowed the Q-switched pulse properties to stabilize. During this simulation, the saved data was down-sample for memory management reasons. Finally, we performed a third simulation of 500 μs duration with a high temporal resolution. This enabled us to analyze the system over the duration of a single pulse.

Simulations were conducted for PRFs ranging between 2.5 kHz and 100 kHz. The pulse duration and energy are illustrated in Fig. 11. The predicted minimum pulse duration and maximum pulse energy occur at a PRF of around 15 kHz and 25 kHz in the case when the first pump operates at 4 W and 2 W respectively . The maximum predicted peak power was 500 W which occurred when the pulse duration was 88 ns and the pulse energy was 44 μJ.

It is expected that the pulse energy increases with decreasing repetition rate for CW-pumped, repeatedly Q-switched laser, until the inverse of the upper state lifetime is reached (177 μs for the ${}^4F_{9/2}$ level in Er^{3+}:ZBLAN [35]). At this point, the increase plateaus. An example can be seen in the low power curve in Fig. 5 of the paper by Chang et al. [40]. The behavior predicted for this DWP system is different in a number of ways. Firstly, the peak energy is achieved around 20 kHz which is considerably higher than the inverse of the upper state lifetime (~ 5 kHz). Secondly, when the peak energy is reached, the energy of the pulses decline as the pulse duration is decreased. This behavior can be explained when the time dependent population of critical states is evaluated.

The time dependent population densities averaged over the fiber are plotted for the cases of 5 kHz and 25 kHz in Figs. 12 and 13 respectively. When the 5 kHz PRF is considered, it becomes apparent that the upper lasing state population saturates well before the end of the pump cycle. This can be explained by the bleaching of the second pump transition. It also means that the pulse energy can be increased by increasing the power of the 977 nm pump since this will increase the population in the ${}^4I_{11/2}$ level and hence increase the saturation intensity of the second pump. The reduction in pulse energy as the PRF decreases can be described by a more subtle effect. In this regime, a slightly higher time average population is maintained in the ${}^4F_{9/2}$ state for the lower repetition rate case. This means more ions can exit this state by spontaneous processes, hence leave the lasing cycle resulting in a reduced population in the ${}^4I_{11/2}$ state. This lowers the saturation intensity of the second pump and reduces the inversion at the time of Q-switching . This simulation demonstrates that for Q-switched operation, higher levels of

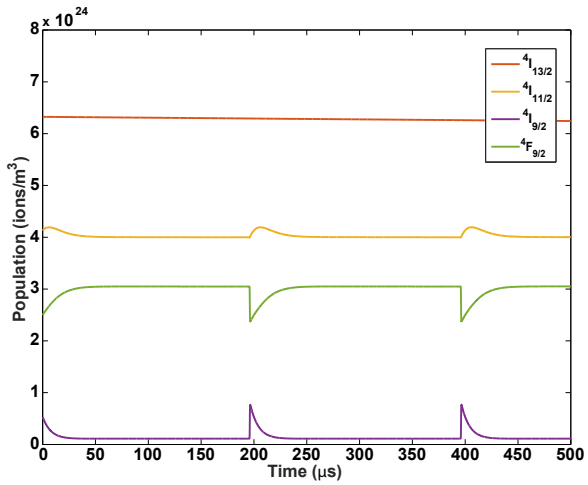

Fig. 12. The time dependent behavior of the spatially averaged population density along the fiber when pulsing at 5 kHz. The power of the 977 nm pump was set to 2 W.

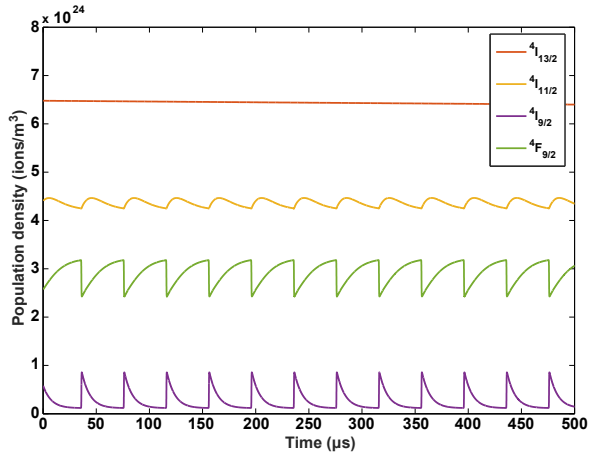

Fig. 13. The time dependent behavior of the spatially averaged population density along the fiber when pulsing at 25 kHz The power of the 977 nm pump was set to 2 W.

the 977 nm pump are highly desirable.

V. Conclusions

In this paper we have reviewed the current state of the art in rare-earth doped mid-infrared fiber lasers with a particular emphasis on systems that utilize dual-wavelength pumping.

We have measured the excited state absorption cross section of the ${}^4I_{11/2} \rightarrow {}^4 F_{9/2}$ transition in erbium using excited state absorption spectroscopy in fibers for the first time. This transition is used when DWP is used to generate lasing emission around 3.5 μm. The data presented shows that the peak absorption of this transition is located at 1973 nm. We used the McCumber relationship to derive the stimulated emission cross section of this transition as well. Accurate knowledge of both the emission and absorption cross section of this transition are important to accurately numerically model the performance of DWP erbium lasers.

We have presented an initial investigation of the remaining steps that will be required to make these DWP lasers suitable for remote hydrocarbon sensing using DiAL. This included a comparison of the fluorescent curves of the 3.5 μm transition for fibers with differing concentrations and ZBLAN formulation. This shows the exciting possibility that it may be possible to extend the performance of the ${}^4F_{9/2} \rightarrow {}^4 I_{9/2}$ to shorter wavelength. Pulsed operation is important for lasers that are used in DiAL, hence we present a numerical investigation of a Q-Switched 3.5 μm laser. This study showed that sub 100 ns duration pulses are theoretically possible with corresponding peak powers of 500 W. This modeling also showed that high levels of 977 nm pump are more important for pulsed operation compared with CW operation to prevent bleaching of the virtual ground state that is established by the 977 nm pump.

Acknowledgments

The authors would like to thank eRSA (South Australian provider of high performance computing) for the provision of computer resources. This research was supported by grants from the South Australian Government through the PRIF and PSRF schemes and The University of Adelaide.

References

[1] B. Molocher, "Countermeasure laser development," in *European Symposium on Optics and Photonics for Defence and Security*. International Society for Optics and Photonics, 2005, p. 598902.

[2] B. M. Walsh, H. R. Lee, and N. P. Barnes, "Mid infrared lasers for remote sensing applications," *J. Lumin.*, vol. 169, pp. 400–405, 2016.

[3] S.-S. Kim, C. Young, B. Vidakovic, S. G. Gabram-Mendola, C. W. Bayer, and B. Mizaikoff, "Potential and challenges for mid-infrared sensors in breath diagnostics," *IEEE Sensors J.*, vol. 10, no. 1, pp. 145–158, 2010.

[4] Y. Yao, A. J. Hoffman, and C. F. Gmachl, "Mid-infrared quantum cascade lasers," *Nat. Photon.*, vol. 6, no. 7, pp. 432–439, 2012, cited By (since 1996): 7 Export Date: 20 March 2013 Source: Scopus.

[5] T. Kruczek, K. A. Fedorova, G. S. Sokolovskii, R. Teissier, A. N. Baranov, and E. U. Rafailov, "InAs/AlSb widely tunable external cavity quantum cascade laser around 3.2 mu m," *Appl. Phys. Lett.*, vol. 102, no. 1, pp. 011 124–3, 2013.

[6] V. Fortin, M. Bernier, S. T. Bah, and R. Valle, "30 W fluoride glass all-fiber laser at 2.94 μm," *Opt. Lett.*, vol. 40, no. 12, pp. 2882–2885, 2015.

[7] S. Tokita, M. Murakami, S. Shimizu, M. Hashida, and S. Sakabe, "12 W q-switched er:zblan fiber laser at 2.8 μm," *Opt. Lett.*, vol. 36, no. 15, pp. 2812–2814, 2012.

[8] S. D. Jackson, "Towards high-power mid-infrared emission from a fibre laser," *Nature Photonics*, vol. 6, no. 7, pp. 423–431, 2012.

[9] V. Fomin, "10 kw single-mode fiber laser," in *5th International Symposium on High-Power Fiber Lasers and Their Applications*, 2010.

[10] Y. Jeong, S. Yoo, C. Codemard, J. Nilsson, J. Sahu, D. Payne, R. Horley, P. Turner, L. Hickey, A. Harker, M. Lovelady, and A. Piper, "Erbium:ytterbium codoped large-core fiber laser with 297-W continuous-wave output power," *IEEE Journal on Selected Topics in Quantum Electronics*, vol. 13, no. 3, pp. 573–578, 2007.

[11] T. Ehrenreich, R. Leveille, I. Majid, K. Tankala, G. Rines, and P. Moulton, "1-kW, all-glass tm:fiber laser," *SPIE Photonics West 2010: LASE Fiber Lasers VII: Technology, Systems, and Applications*, 2010.

[12] A. Hemming, S. Bennetts, N. Simakov, J. Haub, and A. Carter, "Development of resonantly cladding-pumped holmium-doped fibre lasers," in *Proceedings of SPIE 8237*, 2012.

[13] S. Tokita, M. Murakami, S. Shimizu, M. Hashida, and S. Sakabe, "Liquid-cooled 24 w mid-infrared Er^{3+}:zblan fiber laser," *Opt. Lett.*, vol. 34, no. 20, pp. 3062–3064, 2009.

[14] S. Crawford, D. D. Hudson, and S. D. Jackson, "High-power broadly tunable 3-μm fiber laser for the measurement of optical fiber loss," *Photon. J., IEEE*, vol. 7, no. 3, pp. 1–9, 2015.

[15] J. Li, D. Hudson, and S. Jackson, "High-power diode-pumped fiber laser operating at 3 μm," *Opt. Lett.*, vol. 36, no. 18, pp. 3642–3644, 2011.

[16] C. Carbonnier, H. Többen, and U. B. Unrau, "Room temperature CW fibre laser at 3.22 μm," *Electronics Letters*, vol. 34, no. 9, pp. 893–894, 1998.

[17] M. R. Majewski and S. D. Jackson, "Highly efficient mid-infrared dysprosium fiber laser," *Opt. Lett.*, vol. 41, no. 10, pp. 2173–2176, 2016, export Date: 17 July 2016.

[18] V. Fortin, F. Maes, M. Bernier, S. T. Bah, M. D'Auteuil, and R. Vallée, "Watt-level erbium-doped all-fiber laser at 3.44 μm," *Opt. Lett.*, vol. 41, no. 3, pp. 559–562, Feb 2016.

[19] O. Henderson-Sapir, S. D. Jackson, and D. J. Ottaway, "Versatile and widely tunable mid-infrared erbium doped ZBLAN fiber laser," *Opt. Lett.*, vol. 41, no. 7, pp. 1676–1679, Apr 2016.

[20] H. Többen, "Room temperature CW fibre laser at 3.5 μm in Er^{3+}-doped ZBLAN glass," *Electron. Lett.*, vol. 28, no. 14, pp. 1361–1362, 1992.

[21] O. Henderson-Sapir, J. Munch, and D. J. Ottaway, "Mid-infrared fiber lasers at and beyond 3.5 μm using dual-wavelength pumping," *Opt. Lett.*, vol. 39, no. 3, pp. 493–6, Feb 2014.

[22] J. Schneider, "Fluoride fibre laser operating at 3.9 μm," *Electron. Lett.*, vol. 31, no. 15, pp. 1250–1251, 1995.

[23] S. D. Jackson and D. G. Lancaster, *Fiber lasers that bridge the short-wave to midwave regions of the infrared spectrum*, O. G. Okhotnikov, Ed. Wiley-VCH Verlag GmbH & Co. KGaA, 2012.

[24] O. Henderson-Sapir, J. Munch, and D. J. Ottaway, "New energy-transfer upconversion process in Er^{3+}:ZBLAN mid-infrared fiber lasers," *Opt. Express*, vol. 24, no. 7, pp. 6869–6883, Apr 2016.

[25] O. Henderson-Sapir, J. Munch, and D. J. Ottaway, "A higher power 3.5 μm fibre laser," in *Advanced Solid State Lasers*. Optical Society of America, 2014, p. ATu1A.3.

[26] O. Henderson-Sapir, "Development of dual-wavelength pumped mid-infrared fibre laser," Ph.D. dissertation, University of Adelaide, 2015.

[27] A. Malouf, O. Henderson-Sapir, and D. J. Ottaway, "Numerical modeling of 3.5 µm dual-wavelength pumped erbium doped mid-infrared fiber lasers," *(submitted to) IEEE J. of Quantum Electron.*, 2016.

[28] K. Tanimura, M. Shinn, W. Sibley, M. Drexhage, and R. Brown, "Optical transitions of Ho^{3+} ions in fluorozirconate glass," *Phys. Rev. B*, vol. 30, no. 5, p. 2429, 1984.

[29] D. E. McCumber, "Theory of phonon-terminated optical masers," *Phys. Rev.*, vol. 134, no. 2A, pp. A299–A306, 1964.

[30] R. Caspary, "Applied rare earth spectroscopy for fiber laser optimization," Ph.D. dissertation, Technical University of Braunschweig, 2001.

[31] V. Fortin, F. Maes, M. Bernier, and R. Vallée, "Erbium-doped all-fiber laser operating at 3.44 μm: Experimental and numerical studies," in *CLEO: Science and Innovations*. Optical Society of America, 2016, pp. STh1O–3.

[32] M. Pollnau, E. Heumann, and G. Huber, "Time-resolved spectra of excited-state absorption in Er^{3+} doped $YAlO_3$," *Appl. Phys. A*, vol. 54, no. 5, pp. 404–410, 1992.

[33] M. Pollnau, C. Ghisler, W. Lüthy, and H. P. Weber, "Cross sections of excited-state absorption at 800 nm in erbium-doped zblan fiber," *Appl. Phys. B*, vol. 67, no. 1, pp. 23–28, 1998.

[34] P. S. Golding, S. D. Jackson, T. A. King, and M. Pollnau, "Energy transfer processes in Er^{3+}-doped and Er^{3+},Pr^{3+}-codoped ZBLAN glasses," *Phys. Rev. B*, vol. 62, no. 2, p. 856, 2000.

[35] V. K. Bogdanov, "Energy exchange processes in erbium-doped fluoride glasses," Ph.D. dissertation, Victoria University of Technology, 1999.

[36] D. E. McCumber, "Einstein relations connecting broadband emission and absorption spectra," *Phys. Rev.*, vol. 136, pp. A954–A957, Nov 1964.

[37] Y. D. Huang, M. Mortier, and F. Auzel, "Stark level analysis for Er^{3+}-doped ZBLAN glass," *Opt. Mater.*, vol. 17, no. 4, pp. 501–511, 2001.

[38] F. McClung and R. Hellwarth, "Giant optical pulsations from ruby," *J. of Appl. Phys.*, vol. 33, no. 3, pp. 828–829, 1962.

[39] H. Riris, K. Numata, S. Li, S. Wu, A. Ramanathan, M. Dawsey, J. Mao, R. Kawa, and J. B. Abshire, "Airborne measurements of atmospheric methane column abundance using a pulsed integrated-path differential absorption lidar," *Appl. Opt.*, vol. 51, no. 34, pp. 8296–8305, 2012.

[40] N. Chang, N. Simakov, D. Hosken, J. Munch, D. Ottaway, and P. Veitch, "Resonantly diode-pumped continuous-wave and q-switched er: Yag laser at 1645 nm," *Opt. express*, vol. 18, no. 13, pp. 13 673–13 678, 2010.

Ori Henderson-Sapir received his B.Sc. in physics and mathematics from the Hebrew University in Jerusalem, Israel and his M.Eng. from the Tel-Aviv University in Israel where he worked on development of electrically small antennas. He recently received his Ph.D. from the University of Adelaide in South Australia with the Lasers and Optics Group. He is currently dividing his time as an optics and laser engineer with Ellex Medical and as a research associate at the University of Adelaide. His current research interests are mid-infrared sensing and the development of mid-infrared fiber lasers.

Andrew Malouf received his B.Sc. in experimental and theoretical physics from The University of Adelaide in 2013 and was awarded first class Honours in 2015. He is currently a Ph.D. candidate at The University of Adelaide with the Lasers and Optics Group.

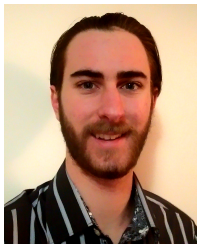

Nathaniel Bawden received his B.Sc. (Laser Physics and Technology) from the University of Adelaide in 2015. He is currently completing an Honours Degree at the University of Adelaide with the Laser and Optics Group.

Jesper Munch received the Ph.D. degree in Physics from the University of Chicago, Chicago, IL, in 1975. He then worked for 17 years at TRW, Redondo Beach, CA, in laser development and nonlinear optics. In 1990, he joined The University of Adelaide, South Australia as the Chair of Experimental Physics and started a lasers and non-linear optics group concentrating on the physics of lasers and their applications, including sodium guide-star lasers and gravitational wave detection, as well as diffractive and nonlinear optics.

Stuart D. Jackson is an associate professor at the Department of Engineering at Macquarie University. He received the BSc(Hons) degree in 1989 from the University of Newcastle (Australia). In 1990, he joined the Centre for Lasers and Applications at Macquarie University to undertake research toward the PhD degree. In 1995, he joined the Laser Photonics Group at the University of Manchester and initiated the research there into high power fiber lasers. Later in 1999, he returned to Australia and joined the Optical Fiber Technology Centre (OFTC) at the University of Sydney where he became a Senior Research Fellow and technical manager of silicate fiber fabrication. During this time, he received an Australian Research Fellowship from the Australian Research Council (ARC). In 2009, he joined the School of Physics at the University of Sydney as a Queen Elizabeth II Fellow (ARC) where he became the Leader of the Flagship Project "Mid-infrared Photonics" within the ARC Centre of Excellence funded Centre for Ultrahigh-bandwidth Devices for Optical Systems (CUDOS). In early 2014, he moved to the Department of Engineering at Macquarie University to take up a permanent position in teaching and optical and photonics engineering research.

David J. Ottaway received the Ph.D. degree from The University of Adelaide, in 1999. His Ph.D. dissertation was on solid state laser sources for gravitational wave detection. In 2000, he joined the LIGO Laboratory, first as a Post-Doctoral Scholar at the LIGO Hanford Observatory, Richland, Washington, and later as a Staff Scientist with the Massachusetts Institute of Technology. During this period, he conducted research on commissioning the Initial LIGO detectors and developing optical and mechanical systems for the advanced LIGO detectors. In 2007, returned to The University of Adelaide, where he continues to develop laser and optical systems for advanced gravitational wave detectors and other forms of extreme remote sensing, including remote trace gas detection and atmospheric temperature studies.